Mon. Not. R. Astron. Soc. **398,** 1254–1262 (2009) doi:10.1111/j.1365-2966.2009.15218.x

The VOISE algorithm: a versatile tool for automatic segmentation of astronomical images

P. Guio★ and N. Achilleos

Physics and Astronomy, University College London, Gower Place, London WC1E 6BT

Accepted 2009 June 9. Received 2009 June 8; in original form 2009 April 7

ABSTRACT

The auroras on Jupiter and Saturn can be studied with a high sensitivity and resolution by the *Hubble Space Telescope* (*HST*) ultraviolet (UV) and far-ultraviolet Space Telescope Imaging Spectrograph (STIS) and Advanced Camera for Surveys (ACS) instruments. We present results of automatic detection and segmentation of Jupiter's auroral emissions as observed by the *HST* ACS instrument with the VOronoi Image SEgmentation (VOISE). VOISE is a dynamic algorithm for partitioning the underlying pixel grid of an image into regions according to a prescribed homogeneity criterion. The algorithm consists of an iterative procedure that dynamically constructs a tessellation of the image plane based on a Voronoi diagram, until the intensity of the underlying image within each region is classified as homogeneous. The computed tessellations allow the extraction of quantitative information about the auroral features, such as mean intensity, latitudinal and longitudinal extents and length-scales. These outputs thus represent a more automated and objective method of characterizing auroral emissions than manual inspection.

Key words: methods: data analysis – methods: numerical – methods: statistical – techniques: image processing.

1 INTRODUCTION

Planetary auroral emission is a particularly useful diagnostic tool for the study of magnetospheric processes. In the polar regions of the planet, currents flow in and out of the upper atmosphere and energetic particles precipitate down the magnetic field lines, impacting on the molecules in the atmosphere. At Jupiter and Saturn, the dominant atmospheric species is hydrogen, which emits in the ultraviolet (UV) when excited by auroral electron impact. In order to observe this UV emission, we need to use a platform above the Earth's absorbing atmosphere, such as the Space Telescope Imaging Spectrograph (STIS) instrument (until the 2004 Saturn campaign), and its successor the Advanced Camera for Surveys (ACS) instrument, both on board the Earth-orbiting *Hubble Space Telescope* (*HST*). From the study of these auroral emissions, we can learn a great deal about magnetospheric processes at these planets without even leaving the Earth orbit (Clarke et al. 2002; Grodent et al. 2003b,a).

The auroras of the outer planets have been studied relatively little in comparison to the Earth's; however, we have advanced our understanding of the environment of Jupiter and Saturn. Jupiter's magnetosphere is the largest cavity in the solar wind flow, i.e. within the heliosphere, and the dynamics of it are largely dominated by the fast rotation of the planet (period $\sim$10 h). It has been established that the most significant component of Jupiter's auroras, the main auroral oval, is driven by planetary rotation. The moon Io orbits deep within Jupiter's magnetosphere (orbital radius $\sim 6R_{\rm J}$, where Jupiter equatorial radius $R_{\rm J} = 71\,492$ km), where it is exposed to large tidal forces as it is subject to the competing gravities of Jupiter and the other Galilean moons: Europa, Ganymede and Callisto. These tidal forces heat the interior of Io, such that it has become extremely volcanic, and liberates from its volcanoes of the order of 1 tonne s^{-1} of sulphur and oxygen plasma into the neighbourhood of its orbit. This plasma feels the fast rotation of Jupiter's magnetic field and is accelerated to the same rotation rate as the planet. This fast rotation causes it to 'diffuse' away from Jupiter due to the centrifugal force, and in doing so it slows down its rotation in an attempt to conserve angular momentum. This results in a vast spinning disc of plasma that corotates with Jupiter in the inner region and more slowly in the outer region. Jupiter's magnetic field, however, attempts to keep all this plasma rotating at the same angular velocity. This enforcement is mediated by an electric current system, one component of which results in electrons bombarding Jupiter's upper atmosphere and causing the main oval auroras (Hill 1979; Vasyliunas 1983).

Jupiter also exhibits two other classes of auroral feature: the moon footprints and the polar auroras. The moon footprints are spots of auroral emission that are magnetically linked to the Galilean moons. The brightest spot is that associated with Io, and it also exhibits a tail, or 'wake' that traces eastwards (in the direction of rotation) around the planet. The exact details of the processes that lead to the

★E-mail: p.guio@ucl.ac.uk

formation of the footprints are still not understood, but it is thought that they are a result of the moons' interaction with the rotating magnetic field and the acceleration of newly created plasma to the speed of the rotating field via Alfvén waves (Gurnett & Goertz 1981; Bonfond et al. 2007). The polar auroras are still somewhat of an enigma, as they are the most highly variable component of Jupiter's auroras in terms of brightness. The location and variation of these auroral emissions make it possible that at least some of them may be caused by the solar wind interaction, although this has yet to be proved conclusively. Interestingly, a recent work (Pallier & Prangé 2001) shows good evidence that Jupiter's polar cap boundary, i.e. the perimeter of the region where planetary field lines open into the solar wind, is coincident at times with some of these polar emissions.

The preceding discussions highlight an important link between the geometrical properties and locations of auroral features, and the physical processes of their origin. Previous observational studies (e.g. Pallier & Prangé 2001) have used correlation techniques (spatial filtering) to emphasize auroral features at selected length-scales. In this paper, we present a new automated technique for producing maps of the entire range of length-scales and other properties of features in a given auroral image.

Segmentation refers to the process of partitioning a digital image into multiple regions (sets of pixels). The goal of segmentation is to simplify and/or change the representation of an image into something that is more physically meaningful and easier to analyse. Image segmentation is typically used to locate objects and boundaries (lines, curves, etc.) in images, and different approaches have been developed especially for the purpose of medical imaging (Pham, Xu & Prince 2000). In the astrophysical context, different methods have also been used in image processing and analysis. Amongst others, we mention the watershed transform (Platen, van de Weygaert & Jones 2007), the adaptive spatial binning (Cappellari & Copin 2003) and Bayesian image reconstruction (Cabrera, Casassus & Hitschfeld 2008).

In this paper, we present the Voronoi Image Segmentation (VOISE) algorithm, a method for segmentation of an image into regions based on the partitioning of the support of the image (the set of data values over all pixels) into a set of disjoint convex polygons. Each polygon is a Voronoi region (VR), and the boundary points of the collection of the VRs are a Voronoi diagram (VD). The VD is sometimes also known as a Dirichlet tessellation, and the VRs are also called Dirichlet regions, Meijering cells, Thiessen polytopes or Voronoi polygons (Okabe et al. 2000). The set of VRs is determined by a finite number of points (one point inside each VR) called *seeds*, sometimes called *germs* or *generators*. VOISE is an iterative and self-organizing algorithm (Jantsch 1980; Nicolis & Prigogine 1989) for automatic segmentation of an image, based on adaptive construction of a VD. It consists of dynamically subdividing and merging a network of convex polygons according to the information contained in the underlying image.

In Section 2, we give a detailed introduction about the VD. In Section 3, the VOISE algorithm is developed. The behaviour of auroras is frequently studied through manual inspection of two-dimensional image data. In Section 4, we apply the VOISE algorithm to images of Jupiter's auroras from the *HST* ACS instrument with the Solar Blind Channel (SBC). In Section 5, we discuss the results of the segmentation. We expect the VOISE algorithm to provide more objective and more efficient analyses than visual inspection, especially when such analysis relies on statistics of large volumes of data, whose manual processing may be prone to human error.

Additional natural byproducts of the VOISE algorithm include compression of data and noise-limited detection of features. These aspects will be explored in a future study. It is the purpose of this paper to introduce the fundamentals of the technique, together with its application in auroral physics study.

2 VORONOI DIAGRAM

The VD is one of a few truly interdisciplinary concepts with relevant material to be found in fields as different as anthropology, astronomy, ecology, physics, and urban and regional planning (Okabe et al. 2000). Let us begin by considering a set of seeds $S = \{\boldsymbol{s}_1, \boldsymbol{s}_2, \ldots, \boldsymbol{s}_n\}$, where $\boldsymbol{s}_i$ are distinct points in the plane $\mathbb{R}^2$. The VR associated with seed $\boldsymbol{s}_i$, noted $\mathcal{R}(\boldsymbol{s}_i)$, is the set of points $\boldsymbol{p}$ in the plane $\mathbb{R}^2$ that are nearer to $\boldsymbol{s}_i$ than to any other seeds $\boldsymbol{s}_j$, with respect to the Euclidean distance d, formally

$$\mathcal{R}(\boldsymbol{s}_i) = \{\boldsymbol{p} \in \mathbb{R}^2 \,|\, d(\boldsymbol{p}, \boldsymbol{s}_i) < d(\boldsymbol{p}, \boldsymbol{s}_j), \quad \boldsymbol{s}_j \in S \backslash \boldsymbol{s}_i\}, \tag{1}$$

and its closure, noted $\overline{\mathcal{R}}(\boldsymbol{s}_i)$, is defined as

$$\overline{\mathcal{R}}(\boldsymbol{s}_i) = \{\boldsymbol{p} \in \mathbb{R}^2 \,|\, d(\boldsymbol{p}, \boldsymbol{s}_i) \leq d(\boldsymbol{p}, \boldsymbol{s}_j), \quad \boldsymbol{s}_j \in S \backslash \boldsymbol{s}_i\}. \tag{2}$$

The VD of a set of seeds S, noted $\mathcal{V}(S)$, is the graph or 'skeleton' formed by the polygonal boundaries of the VRs of all seeds in S, i.e.

$$\mathcal{V}(S) = \bigcap_{\boldsymbol{s}_i \in S} \overline{\mathcal{R}}(\boldsymbol{s}_i). \tag{3}$$

Since the intersection of any VRs is empty and the union of the closure of all VRs is the plane, the VD is called a tessellation of the plane.

In the terminology of mathematical morphology, the VR $\mathcal{R}(\boldsymbol{s}_i)$ is called the *influence zone* or the *dominance region* of $\boldsymbol{s}_i$, and $\mathcal{V}(S)$ the *skeleton by influence zones*. Note that the definitions given in equations (1)–(3) are still valid for any space where a distance has been defined . For instance, in the three-dimensional Euclidean space, the VRs are convex polyhedra and the VD consists of the skeleton formed by the boundaries of the VRs.

Fig. 1 illustrates the VD for a set of eight seeds in the plane. Two seeds are said to be neighbours if their associated VRs share a common edge.

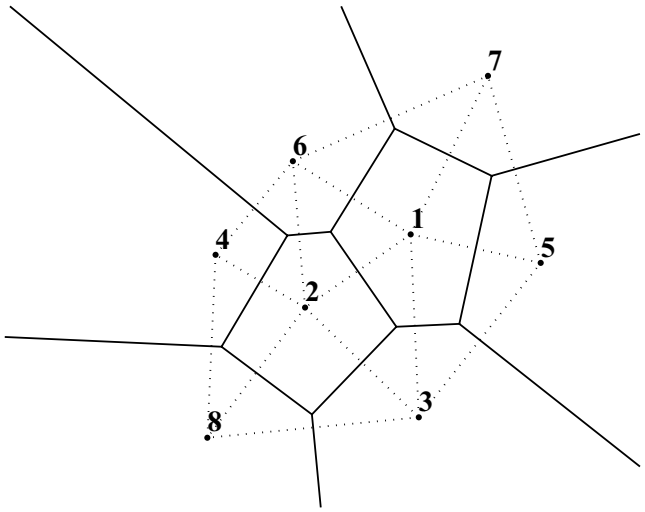

Figure 1. Illustration of a planar VD (solid lines) and its dual DT (dotted lines) of a set S consisting of eight seeds (labelled 1 to 8).

In addition to its geometrical representation, the VD can also be identified by an abstract representation called a Voronoi *graph*. The Voronoi graph is a *planar* graph in two-dimensional space. The graph $G(S) = (V, E)$ represents the topological structure of the neighbouring VRs. The nodes (or vertices) V and lines (or edges) E of the graph G represent, respectively, the seeds and the unordered pairs of nodes that represent links connecting two seeds. In Fig. 1, the neighbours of seed $\boldsymbol{s}_1$ consist of the set $\mathcal{N}(\boldsymbol{s}_1) = \{\boldsymbol{s}_2, \boldsymbol{s}_3, \boldsymbol{s}_5, \boldsymbol{s}_7, \boldsymbol{s}_6\}$. Thus, we can deduce that the pairs $\{\boldsymbol{s}_1, \boldsymbol{s}_2\}$, $\{\boldsymbol{s}_1, \boldsymbol{s}_3\}$, $\{\boldsymbol{s}_1, \boldsymbol{s}_5\}$, $\{\boldsymbol{s}_1, \boldsymbol{s}_7\}$ and $\{\boldsymbol{s}_1, \boldsymbol{s}_6\}$ are links of the graph associated with the node $\boldsymbol{s}_1$.

The data structure consisting of the neighbour list for all seeds $\mathcal{N}(S) = \{\mathcal{N}(\boldsymbol{s}_1), \mathcal{N}(\boldsymbol{s}_2), \ldots, \mathcal{N}(\boldsymbol{s}_n)\}$ thus represents the Voronoi graph.

The set $\mathcal{N}(S)$ also characterizes the Delaunay triangulation (DT), which is obtained by connecting all the pairs of neighbour seeds. The nodes and faces (triangles) of the DT correspond, respectively, to the polygons and nodes of the VD. The DT is called the *dual* graph representation of the primal graph of the VD.

The DT is widely used in various applications such as finite element methods and interpolation schemes, owing to the fact that, once the set of seeds S has been defined, the DT optimizes the geometric 'compactness' of the triangulation. In particular, the DT maximizes the minimum angles of all its element triangles. Also, the DT is the unique triangulation where the circumscribed circle of each triangle does not contain any other vertices.

Also note that a VR may be either a bounded or an unbounded region. When a VR is bounded, the number of edges and vertices is equal, when unbounded there is one vertex less than there are edges. In Fig. 1, the regions, $\mathcal{R}(\boldsymbol{s}_1)$ and $\mathcal{R}(\boldsymbol{s}_2)$, are bounded while all the others are unbounded. The polygon $\mathcal{P}$ consisting of the vertices $\{\boldsymbol{s}_4, \boldsymbol{s}_8, \boldsymbol{s}_3, \boldsymbol{s}_5, \boldsymbol{s}_7, \boldsymbol{s}_6\}$, which are the seeds of all the unbounded regions, is called the convex hull of the set S.

The construction of the VD and the DT is a fundamental problem in computational geometry, and many approaches have been proposed to compute them, such as the incremental method, the divide-and-conquer method and the plane sweep method (Okabe et al. 2000).

An image in this context is a real-valued function $\mathcal{I}(\boldsymbol{p})$ defined for $\boldsymbol{p}$, pixels in the image plane: a two-dimensional lattice space $\Omega \subset \mathbb{N}^2$. In the rest of this paper, we restrict the set of seeds S to be distinct points in the image plane Ω. Accordingly, the VR and VD are defined as their restriction to the image plane Ω.

3 VOISE ALGORITHM

VOISE is an iterative and self-organizing algorithm, and consists of up to four different phases explained hereafter.

3.1 Initialization phase

A small number of seeds are initially *randomly* drawn according to the uniform probability distribution over the image plane Ω, and the corresponding VD is constructed.

The generation of points in space according to a probability distribution is called a stochastic point process. For a uniform probability distribution over a bounded region, the process is the binomial point process, where for any subset of the region, the probability distribution for the number of points within the subset is given by the binomial distribution. Asymptotically, if we let the bounded region tend towards the infinite region $\mathbb{R}^2$ while keeping the density of points constant, the process tends towards the homogeneous Poisson point process and the tessellation is called a Poisson–Voronoi tessellation (Okabe et al. 2000).

The set of VRs represents a 'tiling' of the image plane Ω. Let us consider an operator $f(\mathcal{I}, \boldsymbol{s}_i)$ which associates, to each seed $\boldsymbol{s}_i$, a unique value depending on the region $\mathcal{R}(\boldsymbol{s}_i)$, and the intensity of the image pixels within that region, i.e. the restriction $\mathcal{I}|_{\mathcal{R}(\boldsymbol{s}_i)}$ of $\mathcal{I}$ to $\mathcal{R}(\boldsymbol{s}_i)$, with values in the set $\{\mathcal{I}(\boldsymbol{p}),\ p \in \mathcal{R}(\boldsymbol{s}_i)\}$. Then, a tiled image $\mathcal{T}_f$ can be constructed by 'filling' each polygon with the value given by applying the operator $f(\mathcal{I}, \boldsymbol{s}_i)$, formally

$$\mathcal{T}_f(p) = f(\mathcal{I}, \boldsymbol{s}_i), \quad \text{for} \quad \boldsymbol{s}_i \in S \quad \text{and} \quad p \in \mathcal{R}(\boldsymbol{s}_i). \tag{4}$$

In order to calculate a tiled approximation of an image with a set of seeds S, one can, for instance, use statistical averages such as the arithmetic mean or the median for the operator f.

3.2 Dividing phase

The dividing phase is an iterative process and is the main process for 'evolving' the VD. First, we need to define a measure of *homogeneity* for the set of pixels of the underlying image within each VR of the diagram. We define the merit function χ of the image $\mathcal{I}$ in the region associated with seed $\boldsymbol{s}_i$ as

$$\chi\,(\mathcal{I}, \boldsymbol{s}_i) = \frac{\max\limits_{\boldsymbol{p}\in\mathcal{R}(\boldsymbol{s}_i)} [\mathcal{I}(\boldsymbol{p})] - \min\limits_{\boldsymbol{p}\in\mathcal{R}(\boldsymbol{s}_i)} [\mathcal{I}(\boldsymbol{p})]}{\|\chi(\mathcal{I}, S)\|}, \tag{5}$$

$$\|\chi(\mathcal{I}, S)\| = \max_{\boldsymbol{s}_i \in S} \left\{ \max_{\boldsymbol{p}\in\mathcal{R}(\boldsymbol{s}_i)} [\mathcal{I}(\boldsymbol{p})] - \min_{\boldsymbol{p}\in\mathcal{R}(\boldsymbol{s}_i)} [\mathcal{I}(\boldsymbol{p})] \right\}. \tag{6}$$

The numerator of the right-hand side in equation (5) is a 'max–min' measure of the variation of the image intensity within the region $\mathcal{R}(\boldsymbol{s}_i)$. The numerator, defined in equation (6), is the L-infinity norm of this max–min measure of the image intensity for the entire VD. The values of the measure of homogeneity $\chi\,(\mathcal{I}, \boldsymbol{s}_i)$ are, by definition, bounded in the interval $[0, 1]$. The minimum value of χ corresponds to the most homogeneous VR, and, conversely, the maximum value is for the least homogeneous region. Note that the merit function χ, defined in equations (5) and (6), is only one of many possibilities. Any alternative merit function can easily be plugged in VOISE.

When a cell is not homogeneous according to the chosen homogeneity threshold $\chi_{\rm m}$, i.e.

$$\chi(\mathcal{I}, \boldsymbol{s}_i) \geq \chi_{\rm m}, \tag{7}$$

seeds are added within this region. The number of seeds added corresponds to the number of vertices in the polygon. Each added seed is the barycentre of the seed of the VR with weight $w_{\rm s}$, and a vertex of the polygon with weight $w_{\rm v}$, corresponding to a fixed relative distance from the seed. The most probable number of vertices/edges of a typical cell of a Poisson–Voronoi diagram is six (Okabe et al. 2000); in other words, the most probable polygon is an hexagon. Fig. 2 illustrates the method for three iterations starting with the hexagon in the centre of the upper-left panel and iteratively over the innermost hexagon, adding six seeds at each iteration, and for three weightings, ($w_{\rm s} = 1/4$, $w_{\rm v} = 3/4$) in the upper-right panel, ($w_{\rm s} = 1/2$, $w_{\rm v} = 1/2$) in the lower-left panel and ($w_{\rm s} = 3/4$, $w_{\rm v} = 1/4$) in the lower-right panel. In the last case where the seeds are added nearest to the seed of the original region, the newly created central region is very small compared to the newly created surrounding regions. In VOISE, we set these parameters to $w_{\rm s} = 5/8$ and $w_{\rm v} = 3/8$ which provides a good compromise between quick convergence and comparable size of new regions.

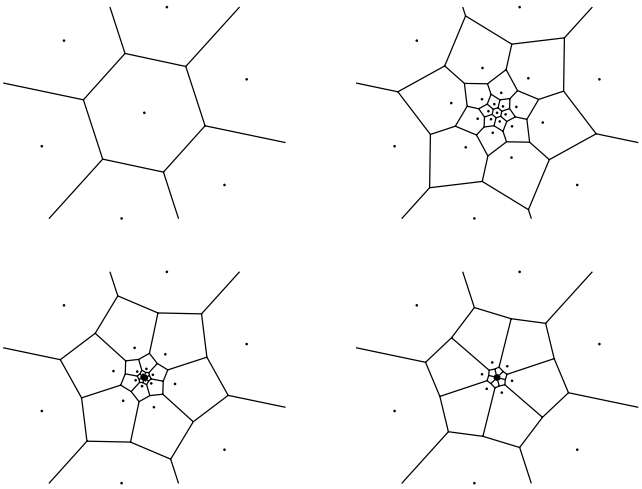

Figure 2. Illustration of the method to add seeds for different weightings. Seeds are added to the central hexagonal region (upper-left panel) recursively for three iterations, adding 18 seeds. The weights are $w_s = 1/4$, $w_v = 3/4$ (upper-right panel), $w_s = 1/2$, $w_v = 1/2$ (lower-left panel) and $w_s = 3/4$, $w_v = 1/4$ (lower-right panel).

This iterative and deterministic algorithm of adding new seeds ensures the regular growth of regions such that self-similar structure across different length-scales is emphasized (fractals with recursive definition, such as the Koch flake, are classic examples of self-similarity).

The threshold χ_m is a *dynamic* and *self-organizing* parameter estimated for each new iteration of a dividing phase using quantile statistics on the sample χ_i of the measure of homogeneity, i.e.

$$\chi_i = \{\chi(\mathcal{I}, \boldsymbol{s}_i), \boldsymbol{s}_i \in S\}. \tag{8}$$

χ_m is defined as the value of the homogeneity measure for which a fraction $p_D/100$ of the polygons are homogeneous, i.e. such that $\chi(\mathcal{I}, \boldsymbol{s}_i) < \chi_m$. Thus, defining the probability Prob, that a given polygon has its value $\chi(\mathcal{I}, \boldsymbol{s}_i)$ below the threshold χ_m, we can write the following:

$$\mathrm{Prob}\,[\chi(\mathcal{I}, \boldsymbol{s}_i) < \chi_m] = \frac{p_D}{100}. \tag{9}$$

Simultaneously, the probability that a given polygon has its value $\chi(\mathcal{I}, \boldsymbol{s}_i)$ exceeding the threshold χ_m is given by

$$\mathrm{Prob}\,[\chi(\mathcal{I}, \boldsymbol{s}_i) \geq \chi_m] = 1 - \frac{p_D}{100}. \tag{10}$$

The value χ_m is obtained at each iteration as the inverse of the cumulative histogram of the sample χ_i for the value p_D (see middle panel in Fig. 5). Since the cumulative histogram is a monotonic increasing function, smaller values for p_D give smaller value for the threshold χ_m and conversely.

Note that as the subdividing process takes place, the norm $\|\chi(\mathcal{I}, S)\|$ is becoming smaller, and the measure of homogeneity is becoming more stringent. The set of homogeneity measures will accumulate towards the superior value $\sup(\chi) = 1$. The dividing phase is iterated until all VRs are classified as homogeneous, *or* the size of the polygon does not allow the further addition of new seeds. This is characterized by enforcing a minimum distance d_m between two seeds.

For a large value p_D of the percentile (70–80 per cent), the threshold χ_m increases, and thus the dividing scheme will only apply to the $(100 - p_D)$ per cent most inhomogeneous regions according to the merit function χ. With the merit function defined as in equation (5), a large value of p_D will only allow the dividing process to lock on to the most contrasted regions and will not necessarily be able to detect low-contrasted or noisy features of the image. Conversely, for a small value p_D of the percentile (60–70 per cent), the dividing process will be more systematic and uniform over the entire image, but will not account for the most contrasted features of the image. However, it is important to emphasize that the VOISE algorithm is not limited to the present merit function given by equations (5) and (6). Any other merit function that would help characterize a feature, for example texture, noise properties, etc. can be employed in the algorithm instead of the ones given by equations (5) and (6).

The minimum distance d_m between seeds is the parameter which limits the length-scale of the features one wishes to detect. This parameter should be chosen according to the size of the smallest resolvable features.

3.3 Merging phase

At this stage, any VR is either homogeneous with respect to the prescribed threshold χ_m, *or* its shape does not allow us to add any new seed as described in the previous section and fulfil the minimum distance requirement d_m between neighbouring seeds.

The merging phase is also an iterative process. It consists of removing unnecessary 'fine' regions where adjacent VRs have very similar characteristics, for example the averaged intensity μ_i of the image for the region associated with seed $\boldsymbol{s}_i$ as calculated by equation (4) with a specified operator f, in the following the median of the set of values.

A seed $\boldsymbol{s}_i$ is defined as redundant and ought to be removed when the following conditions are fulfilled.

(i) The region $\mathcal{R}(\boldsymbol{s}_i)$ is homogeneous with respect to a chosen homogeneity threshold χ_m, i.e.

$$\chi(\mathcal{I}, \boldsymbol{s}_i) < \chi_m. \tag{11}$$

The value for the threshold is estimated at each iteration from the cumulative histogram of the merit function sample χ_i from a prescribed p_Mth percentile, in the same way as for p_D in Section 3.2

$$\mathrm{Prob}\,(\chi(\mathcal{I}, \boldsymbol{s}_i) < \chi_m) = \frac{p_M}{100}. \tag{12}$$

(ii) Amongst its neighbouring seeds $\boldsymbol{s}_j \in \mathcal{N}(\boldsymbol{s}_i)$ that are embedded in homogeneous region, the relative difference between the averaged values μ_i and μ_j is less than a prescribed threshold $\Delta\mu$, formally

$$|\mu_i - \mu_j| < \Delta\mu|\mu_i|. \tag{13}$$

Two such regions are said to be identical with respect to the averaged intensity μ.

(iii) The total length $\mathcal{L}$ of the edges shared with non-homogeneous neighbours normalized to the perimeter $\mathcal{P}$ of the region does not exceed a prescribed threshold $\Delta\mathcal{H}$, formally

$$\mathcal{L}/\mathcal{P} < \Delta\mathcal{H}. \tag{14}$$

At each iteration, all seeds are checked for redundancy and removed when fulfilling the three conditions above. After a set of seeds has been removed, some regions have grown to absorb the seeds that have been removed. In such regions, the merit function χ can only increase (and may become non-homogeneous), and the averaged intensity is changing. Thus during the merging process, the three conditions become more difficult to fulfil for any seeds and the process stops by itself ('self-regulating').

The percentile of the merging phase, p_M, does not need to be identical to the percentile of the dividing phase, p_D, but should be larger in order to relax the homogeneity criteria and conversely smaller in order to strengthen the homogeneity criteria (see Fig. 5).

The merging phase does not disturb the overall representation of the image but provides a better approximation with fewer seeds. When a seed is removed, the neighbouring polygons reorganize themselves to fill the region associated with the removed seed. We noted that the polygons tend to organize according to the geometrical shapes in the image. The final organization is made independent of the initialization phase by using the merging phase.

Our tests on the image presented in the next section show that different initial distributions of seeds do not significantly change the final VD. Typically, the number of polygons, i.e. the number of seeds in the final VD, is affected by less than 4–5 per cent. The typical difference in area of the VRs for different realizations is less than 10–30 pixels^2. The typical difference in intensity is less that 5–10 per cent. Here, we computed the difference in area of the VRs between two realizations as follows. In a given realization R_1 of the VOISE algorithm, each polygon $\mathcal{R}(\boldsymbol{s}_i^1)$ with seed $\boldsymbol{s}_i^1$ has an area $\mathcal{A}_i^1$. To compute the difference in polygon area between R_1 and a second realization R_2, we determine for each seed $\boldsymbol{s}_i^1$ from R_1, the polygon $\mathcal{R}(\boldsymbol{s}_j^2)$ from R_2, with seed $\boldsymbol{s}_j^2$ and area $\mathcal{A}_j^2$ which contains this seed, i.e. such that $\boldsymbol{s}_i^1 \in \mathcal{R}(\boldsymbol{s}_j^2)$. The difference in area is then $|\mathcal{A}_i^1 - \mathcal{A}_j^2|$.

3.4 Regularization phase

The tessellation obtained from the divide-and-merge phase can be 'regularized' through an iterative relaxation process. This is achieved by computing iteratively a new VD where each seed $\boldsymbol{s}_i$ is replaced by the mass centroid (centre of mass) $\boldsymbol{\xi}_i$ of the polygon $\mathcal{R}(\boldsymbol{s}_i)$ with a density function ρ

$$\boldsymbol{\xi}_i = \frac{\sum_{\boldsymbol{p}\in\mathcal{R}(\boldsymbol{s}_i)} \boldsymbol{p}\rho(\boldsymbol{p})}{\sum_{\boldsymbol{p}\in\mathcal{R}(\boldsymbol{s}_i)} \rho(\boldsymbol{p})}. \tag{15}$$

When the position of each seed coincides with the centre of mass of the polygonal region, the partitioning is called a centroidal Voronoi diagram (CVD) tessellation and the method is known as Lloyd's method. The CVD corresponds to an optimally regular and uniform tessellation with a minimum-energy configuration, in the sense that it minimizes the norm of the second-order inertial moment of each polygon. Asymptotically, the CVD approaches a uniform hexagonal-like lattice (Du, Faber & Gunzburger 1999) for constant density function.

The density function ρ has an important role in the regularization as it is seen in Du et al. (1999). Let us consider the case where the image itself is used as density function, i.e. $\rho(\boldsymbol{p})$ is the value of the image data in the pixel at position $\boldsymbol{p}$. After the dividing and merging phases, the polygons are distributed such that they minimize the merit function χ defined in equations (5) and (6), and the associated density function should be, to a good approximation, constant within each polygon.

Note that the regularization process is controlled in two manners. The iteration process stops by itself when the relative distance between the centre of mass and the seed of any region, i.e.

$$|\boldsymbol{\xi}_i - \boldsymbol{s}_i| \quad \text{for all} \quad \boldsymbol{s}_i \in S, \tag{16}$$

is less than 1 pixel. 1 pixel is enough since the positions of the centres of mass are rounded off to an integer number in order to be in the image plane Ω. In addition, and if required, it is possible to specify a maximum number of iterations of the relaxation process.

The regularization scheme could also be used as a preconditioning to the first iteration(s) of the dividing phase. Following the initialization phase where a limited number of seeds are drawn randomly, a regularization phase with the image as density function tends to move the seeds to positions where the image data tend to form local 'peaks'.

3.5 Implementation

Note that due to the dynamic nature of the algorithm where seeds are added and removed, it would be quite inefficient to construct the entire VD every time the seed configuration is modified, and a more efficient approach is to use an incremental algorithm which operates only on a given seed and its neighbours (see Fig. 2). In addition, the VRs are needed for the points in the image plane, which consists of a discrete and well-organized set of points. We have chosen to use an incremental algorithm for discrete VD using a structure similar to the one described in Sequeira & Preteux (1997), which is designed for seeds located on the image plane Ω, i.e. at discrete positions.

VOISE requires a set of parameters to be initialized. These consist of p_D and d_m for the dividing phase, p_M, $\Delta\mu$ and $\Delta\mathcal{H}$ for the merging phase, and an optional maximum number of iterations for the regularization phase, corresponding to partial regularization.

4 APPLICATION TO *HST* IMAGE

Jupiter's UV auroras have been observed for many years, but recently high-resolution images using the *HST* STIS and ACS instruments have revealed highly dynamic auroral emissions that are controlled to a significant degree by the solar wind (Clarke et al. 2002; Nichols et al. 2008).

Fig. 3 shows an image of Jupiter's UV auroral emission in the Northern hemisphere taken on 2007 February 21 at 16:03:58 UT and projected on to a northern polar view.

The raw data were collected with the SBC channel of the ACS through the F125LP long-pass filter, with short wavelength cut-off of 125 nm. This filter mostly excludes the H Lyman α band. The instrument consists of a 1024×1024 MultiAnode Microchannel Array detector with an average scale of $\sim$0.032 arcsec pixel^{-1}, such that the overall field of view is 35×31 arcsec^2. During each 100 s exposure, the blurring introduced by planetary rotation of any corotating features is $\sim 1^\circ$ at the central meridian longitude (CML). The raw images are reduced: corrected for geometric distortion and scaled to 0.0250 arcsec pixel^{-1}, flat-fielded and dark-count calibrated using the latest calibration files available from the Space Telescope Science Institute. The images are then converted from counts pixel^{-1} to kR of H_2 and Lyman α emission (where 1 kR represents a photon source flux of 10^9 cm^{-2} s^{-1} radiating into 4π steradians) using the conversion factor 1 kR $= 1.473 \times 10^{-3}$ counts s^{-1} pixel (Nichols et al. 2008).

The image in Fig. 3 is a reduced polar projection computed using the metadata provided with the original image and the NASA Navigation and Ancillary Information Facility SPICE system (Acton 1996), and assuming that the light emission is from an infinitesimally thin shell located 200 km above the 1 bar level. The 1 bar level corresponds to a oblate spheroid of eccentricity 0.3 and semimajor axis 71 492 km.

The CML of Jupiter at the time of the observation is 166.°77. The orientation of the image is such that the x-axis corresponds to the

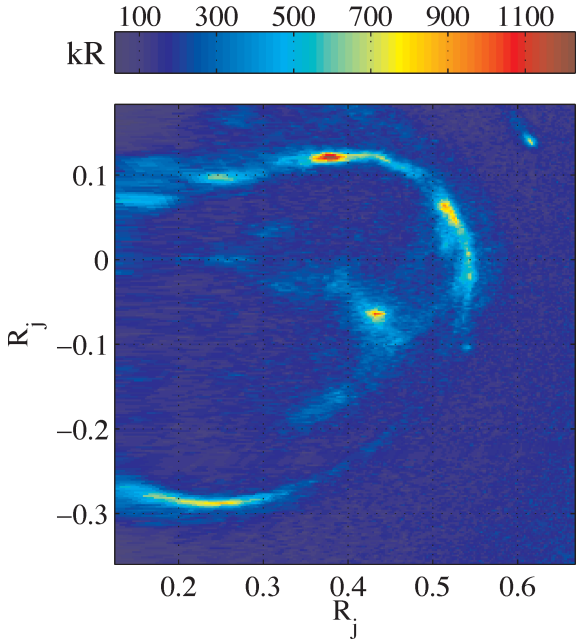

Figure 3. Subimage extracted from the polar projection of Jupiter's UV auroral emission computed from an *HST* ACS/SBC image taken on 2007 February 21 at 16:03:58 UT. The size of the image is 256 × 256 pixels, and the axis units are expressed in Jupiter's equatorial radius (71 492 km). The origin corresponds to the projection of the northern rotational pole of Jupiter and the colour-coded intensity is in kR.

CML meridian, and the dimensions along the axes are in units of Jupiter's radius ($R_J = 71\,492$ km).

A non-continuous auroral oval is clearly identified, as well as several patches of emission within associated with plasma injection and particle precipitation. The footprint of Io is seen in the upper-right part of the image at coordinates $(0.6R_J, 0.15R_J)$. The footprint of the magnetospheric cusp is seen at $(0.4R_J, -0.05R_J)$.

Fig. 4 illustrates the result for the three phases: dividing, merging and regularization of the VOISE algorithm applied to the *HST* image presented in Fig. 3. The 'tiled' images are constructed by filling each polygon with the median value of the pixels that lie within each polygon, and the VD consists of the black solid lines. The VD was initialized with 12 random seeds.

The upper image shows the result of the dividing phase. The minimum distance between two seeds was set to $d_m^2 = 7$ pixels^2 and the homogeneity of the VD by a requirement of a percentile $p_D = 85$ per cent. The percentile $p_D = 85$ per cent is directly read from the ordinate of the cumulative histogram of the sample χ_i in the middle panel of Fig. 5, and the corresponding χ_m is read from the abscissa. The legend gives the iteration number and the number of seeds for the corresponding histogram. The dividing phase converged with the prescribed parameters in 27 iterations and about 950 seeds, as seen in the top panel of Fig. 5. Initially, the cumulative histogram has the signature of a uniform probability distribution, and as the dividing process takes place it converges to a probability distribution where most of the regions ($p_D = 85$ per cent) have their homogeneity criteria $\chi < \chi_m \sim 0.25$.

The middle image shows the result of the merging phase. The threshold for relative similarity is $\Delta\mu = 20$ per cent, the ratio of non-homogeneous boundaries is set to $\Delta\mathcal{H} = 30$ per cent and the homogeneity of the VD is set to a prescribed percentile $p_M =$ 50 per cent. As for the dividing phase, the percentile p_D is directly read in the ordinate of the cumulative histogram of the merit function χ in the middle panel of Fig. 5, and the corresponding χ_m is read in the abscissas. The merging phase consists of seven iterations

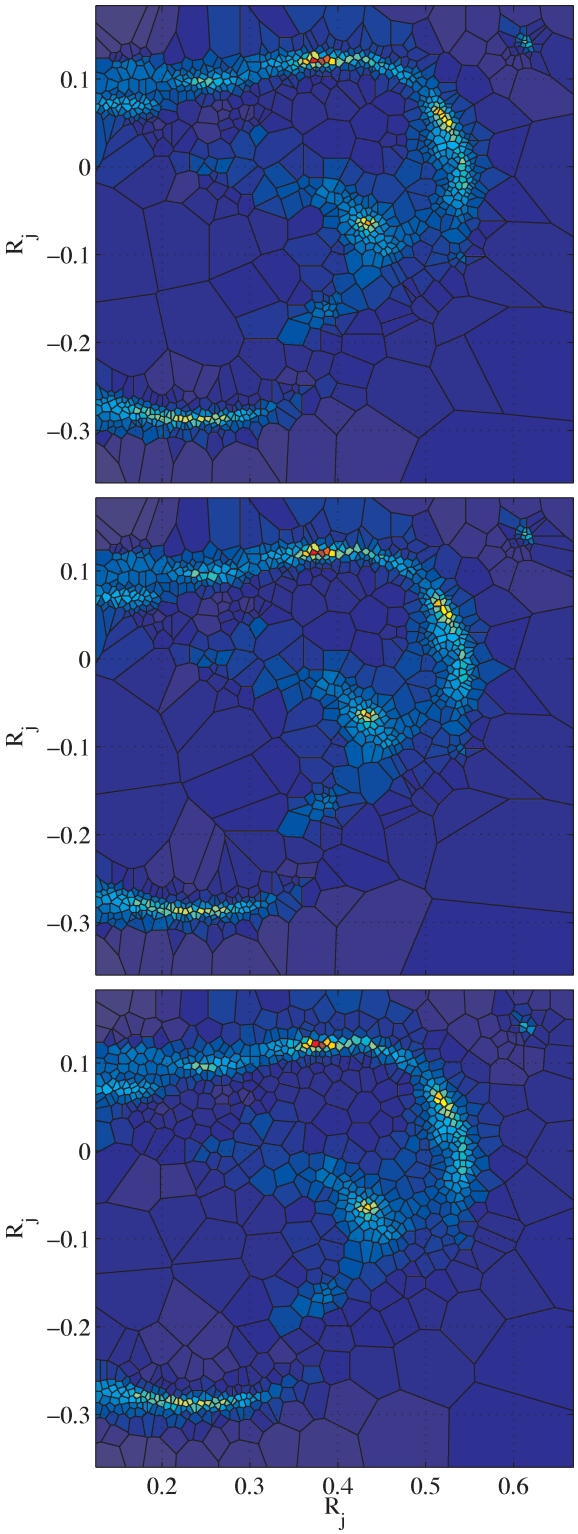

Figure 4. Illustration of the VOISE segmentation algorithm on the image shown in Fig. 3. Top panel: result of the dividing phase; middle panel: result of the merging phase and bottom panel: result of the regularization phase.

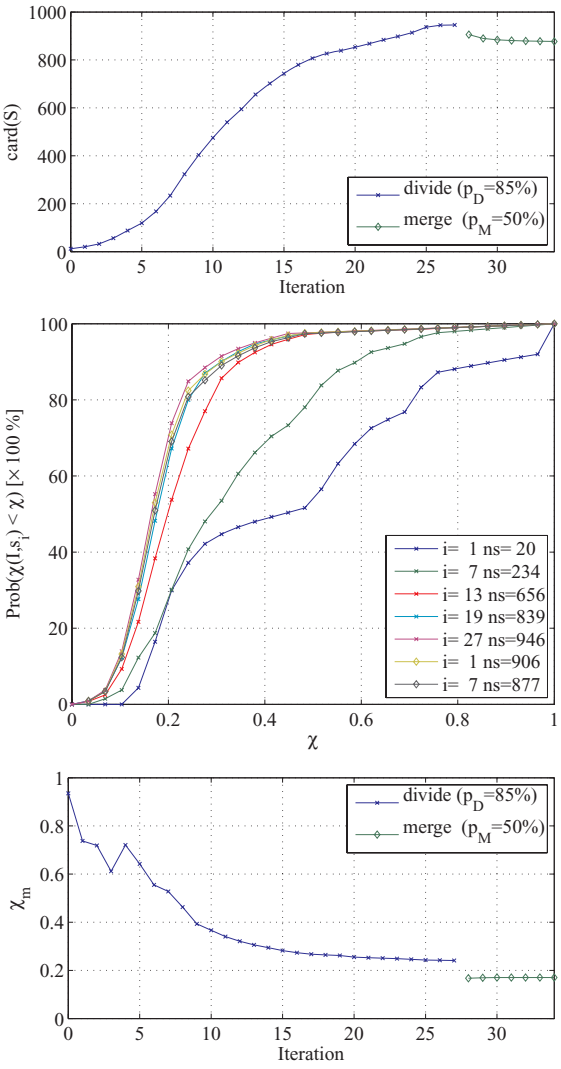

Figure 5. Top panel: the number of seeds, card (S), as function of iteration; middle panel: the cumulative histogram of the sample χ_i associated with the homogeneity merit function χ, as defined in equations (5) and (6), for a selection of iterations of dividing and merging phases. These iterations are labelled in the legend together with the number of seeds; bottom panel: the threshold $\chi_{\rm m}$ derived from the cumulative histogram with the prescribed $p_{\rm D} = 85$ per cent and $p_{\rm M} = 50$ per cent as function of iteration. Solid lines with cross markers refer to dividing phase data, while solid lines with diamond markers refer to merging phase data.

after which the process stops by itself, as no seeds can fulfil the redundancy conditions described.

The lower image shows the result of the regularization phase. The tessellation results from two relaxation iterations, i.e. replacing the seed of each polygon by the centre of mass of the associated region twice. Our experience shows that one or two iterations are in general enough, due to the rounding off of the coordinates of the centre of mass, given by equation (15), to integer values corresponding to points of the image plane Ω.

It is worth noting that the VOISE algorithm based on a statistical distribution of seeds evolves dynamically according to self-organizing of the information in the image as represented by the changing homogeneity threshold $\chi_{\rm m}$.

5 DISCUSSION

Note that any quantity or measure could be calculated for each VR, based on either the properties of the polygons, the statistical properties of the underlying image or a combination of both.

Many analytical properties of the VR have been determined assuming a Poisson–Voronoi tessellation. These include the probability distribution of the perimeter segments, of the angles at the vertices, the polygon area, the polygon to be n-sided, to name a few (Okabe et al. 2000; Hilhorst 2008). Any deviation of the statistics of a property of the VD from the probability distribution of the Poisson–Voronoi tessellation is an indication of seed distribution related to some real point pattern, or clustering as defined in Kaufman & Rousseeuw (2005).

Such 'tiled' images can thus be used to extract quantitative information about structures present in the image, but also potentially to clean an image from unwanted parts such as contamination or defects.

Fig. 6 shows the length-scale calculated as the square root of the number of pixels in each Voronoi polygon times the edge of a pixel in units of 100 km at the planet. This map of length-scales allows post-processing such as selection of points or regions of the image according to a prescribed rule.

Fig. 7 shows the spatial distribution of the seeds of the VD of the middle panel of Fig. 4 in Cartesian and polar coordinate systems. Let us consider a group of neighbouring seeds, i.e. where each polygon in the group shares at least one edge with another polygon. Such group of seeds is defined as a cluster if the polygons in the group are similar with respect to a given property, or combination of properties (Kaufman & Rousseeuw 2005). Such properties could be, for example, purely geometrical (e.g. area, perimeter, length-scale) or related to data values from the underlying image inside polygons (e.g. median intensity, mean intensity). It is important to point out that geometrical properties need not be used, although they would be a natural choice for detection of auroral

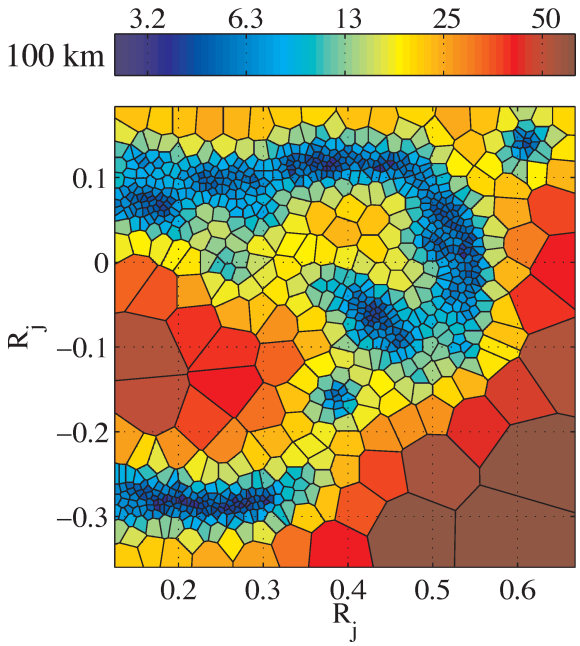

Figure 6. Length-scale estimated from the geometry of the Voronoi polygons obtained after regularization (bottom panel in Fig. 4). The length-scale within a VR is defined as the square root of the area of the polygon. The length-scale is colour-coded in logarithmic scale.

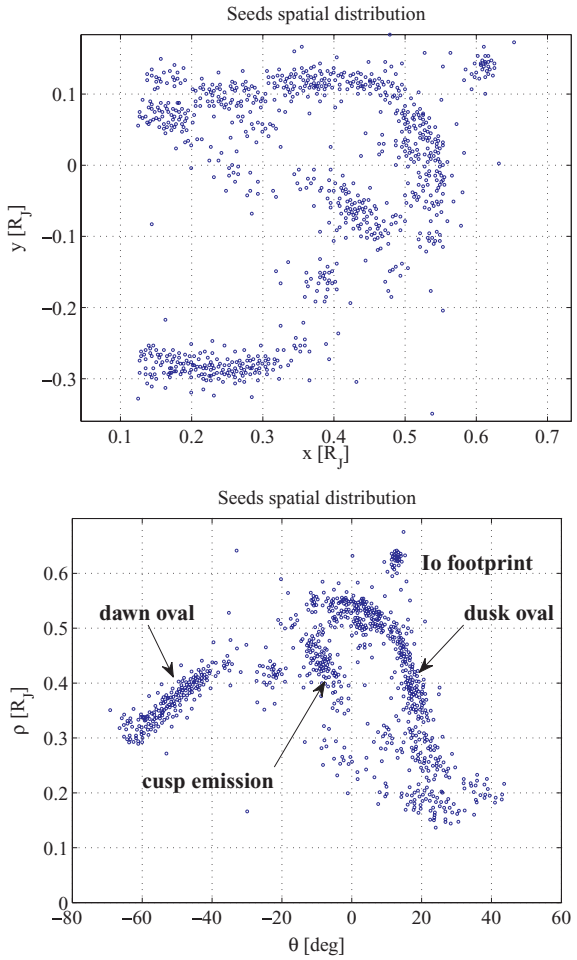

Figure 7. Spatial distribution of the seeds for the segmentation obtained the merging phase (middle panel in Fig. 4) expressed in Cartesian (upper panel) and in polar (lower panel) coordinate systems.

features. Four such clusters with similar median intensity and length-scales are identifiable and annotated in the polar coordinate system: (i) the footprint of Io, (ii) the dusk side segment of the main auroral oval, (iii) the dawn side segment of this oval and (iv) a structure associated with cusp emission. The number of polygons per unit area could be considered a crude representation of the 'density of information' for the image.

Our experiments with mapping polar emissions have frequently detected arc-like auroral features inside the main oval, but running almost parallel to it. These will be the subjects of another study. However, they are similar to the auroral signatures of the polar cap boundary discussed by Pallier & Prangé (2001).

It is interesting to note that the clustering 'compactness' of the seeds is dependent on the coordinate systems. For instance, the footprint of Io in the upper-right corner appears more clustered in polar coordinates. The scattered and relatively low number of seeds allows the high compression of information (with loss) achieved by the VOISE tessellation. The original size of the image shown in Fig. 3 is 256 × 256 pixels with pixel intensity coded over 4 bytes, thus requiring $256^2 \times 4$ bytes. The tessellation contains 877 points. Coding the median intensity over 4 bytes and each coordinate over 2 bytes requires $877 \times (4 + 2 + 2)$ bytes, leading to a compression factor of 37; alternatively coding the coordinates over 4 bytes reduces the compression factor to 25. Quantitative estimates of parameters or features, such as discontinuities in the auroral oval, bifurcation of auroral arcs, polar cap position, footprint of moons, could easily be obtained by fitting the scattered relevant seeds to an analytical model. Some of these features are indicated in Fig. 7. The automatic detection of the limb of the planet to locate accurately and objectively the centre of the planet disc is another potential for application of the VOISE algorithm.

A common concern that runs through a wide range of disciplines is the examination of the spatial occurrence of a particular phenomenon, or *point patterns*, such as *clustering analysis* (Kaufman & Rousseeuw 2005). The analysis of point patterns of the seeds (or spatial occurrence) can be done to divide the VD into component parts. For instance, it was suggested that individual points may be considered to belong to one of the five types: isolated points, members of a curvilinear structure, members of a cluster with an empty interior, or members of either the boundary or the interior of a non-empty cluster (Okabe et al. 2000). The edges of the polygons here aid this classification.

Another application is multitemporal or multisource image analysis and especially the detection of event defined as a structure modification between two images. This can be achieved by comparing the VD of two images generated by VOISE according to the following definition.

Let us consider two sets of seeds S_1 and S_2 and their associated VD. Two seeds, $\boldsymbol{s}_i \in S_1$ and $\boldsymbol{s}_j \in S_2$, are *equivalent* seeds when the seed $\boldsymbol{s}_i$ belongs to $\mathcal{R}(\boldsymbol{s}_j)$, and simultaneously the seed $\boldsymbol{s}_j$ belongs to $\mathcal{R}(\boldsymbol{s}_i)$. The regions associated with seeds $\boldsymbol{s}_i$ and $\boldsymbol{s}_j$ are identical or equivalent when the averaged intensities μ_i and μ_j of the two images for the region associated with seed $\boldsymbol{s}_i$ and $\boldsymbol{s}_j$ are similar with respect to an imposed threshold, while an event is detected between the two images if the averaged intensities are not similar. The application to the analysis of auroral features and their temporal variability is evident, and will be pursued in future studies.

6 CONCLUSION

We have presented VOISE, a self-organizing dynamic algorithm for the automatic segmentation of an image based on adaptive construction of a VD according to some information contained in the underlying image.

The VOISE algorithm has been applied to the detection of UV auroral emission regions on Jupiter as observed by the ACS/SBC instrument on board the *HST*.

In a following paper, we plan to do a statistical survey of the length-scales, morphologies and variability of the auroras for an extensive set of *HST* ACS/SBC images of Jupiter, and look for scale-invariant characteristics, a property of dynamic systems known as self-organized criticality. At present, sequences of typically about 18 images (covering time intervals about or less than 2 hours) are available for 55 different days during the year 2007, providing many different views of both the northern and southern UV auroras. The geometrical nature of auroral emissions is known to be linked with their physical origin. Bright concentrated 'arcs' are the result of strong electric currents flowing between the ionosphere and magnetosphere, while more extended, diffuse emissions arise from scattering of the magnetospheric particles on to trajectories which intercept the planetary atmosphere. Since the macroscopic behaviour of the solar wind displays spatial and temporal scale invariance which is characteristic of self-organized criticality (Chapman et al. 1998; Chapman & Watkins 2001), one would expect similar macroscopic behaviour of the auroral activity to exhibit related spatial and temporal scale invariance.

The VOISE algorithm could easily be extended to three-dimensional data (discrete volume composed of voxels) to perform automatic volume segmentation.

The applicability of the VOISE algorithm is not limited to segmentation of auroral images, but can in practice be used for any types of image data with a suitable homogeneity merit function.

ACKNOWLEDGMENTS

This work is based on the observations with the NASA/ESA *HST*, obtained at the Space Telescope Science Institute, which is operated by AURA for NASA.

We thank the *HST* auroral campaign team the Planetary Atmospheres and Space Science Group at the Boston University for providing the data of Jupiter and for fruitful discussions in the presented method.

We also would like to thank the referee for helpful suggestions and comments.

REFERENCES

Acton C. H., 1996, Planet. Space Sci., 44, 65
Bonfond B., Gérard J.-C., Grodent D., Saur J., 2007, Geophys. Res. Lett., 34, 6201
Cabrera G. F., Casassus S., Hitschfeld N., 2008, AJ, 672, 1272
Cappellari M., Copin Y., 2003, MNRAS, 342, 345
Chapman S., Watkins N., 2001, Space Sci. Rev., 95, 293
Chapman S. C., Watkins N. W., Dendy R. O., Helander P., Rowlands G., 1998, Geophys. Res. Lett., 25, 2397
Clarke J. T. et al., 2002, Nat, 415, 997
Du Q., Faber V., Gunzburger M., 1999, Soc. Industrial Applied Math. Rev., 41, 637
Grodent D., Clarke J. T., Kim J., Waite J. H., Cowley S. W. H., 2003a, J. Geophys. Res., 108, 1389
Grodent D., Clarke J. T., Waite J. H., Cowley S. W. H., Gérard J.-C., Kim J., 2003b, J. Geophys. Res., 108, 1366
Gurnett D. A., Goertz C. K., 1981, J. Geophys. Res., 86, 717
Hilhorst H. J., 2008, European Phys. J. B, 64, 437
Hill T. W., 1979, J. Geophys. Res., 84, 6554
Jantsch E., 1980, Self Organizing Universe: Scientific and Human Implications of the Emerging Paradigm of Evolution. Pergamon Press, Oxford
Kaufman L., Rousseeuw P. J., 2005, Finding Groups in Data. An Introduction to Cluster Analysis, 2nd edn. Wiley-Interscience, New York
Nichols J. D., Clarke J. T., Cowley S. W. H., Duval J., Farmer A. J., Gérard J.-C., Grodent D., Wannawichian S., 2008, J. Geophys. Res., 113, 11205
Nicolis G., Prigogine I., 1989, Exploring Complexity. An Introduction. Freeman & Co., New York
Okabe A., Boots B., Sugihara K., Chiu S. N., 2000, Spatial Tessellations: Concepts and Applications of Voronoi Diagrams, 2nd edn. Wiley, Chichester
Pallier L., Prangé R., 2001, Planet. Space Sci., 49, 1159
Pham D. L., Xu C., Prince J. L., 2000, Ann. Rev. Biomedical. Eng., 2, 315
Platen E., van de Weygaert R., Jones B. J. T., 2007, MNRAS, 380, 551
Sequeira R. E., Preteux F. J., 1997, IEEE Trans. Pattern Analysis Machine Intelligence, 19, 1165
Vasyliunas V. M., 1983, Plasma Distribution and Flow, Physics of the Jovian Magnetosphere. Cambridge Univ. Press, Cambridge

This paper has been typeset from a TEX/LATEX file prepared by the author.